Check for updates

Hydrothermal fluid evolution in the Cuonadong Sn−W−Be polymetallic deposit, southern Tibet: indicated by the in−situ element and boron isotope compositions of tourmaline

Guozhi Xie[1,2,3], Haibo Yan[4], Rongqing Zhang[5], Kun Wang[1,2,3] and Lipeng Zhang[1,2,3]*

[1]Center of Deep-Sea Research, Institute of Oceanology, Chinese Academy of Sciences, Qingdao, China, [2]University of Chinese Academy of Sciences, Beijing, China, [3]Laboratory for Marine Geology, Laoshan Laboratory, Qingdao, China, [4]CAS Key Laboratory of Mineralogy and Metallogeny, Guangzhou Institute of Geochemistry, Chinese Academy of Sciences, Guangzhou, China, [5]Frontiers Science Center for Critical Earth Material Cycling, Nanjing University, Nanjing, China

The Cuonadong Sn−W−Be polymetallic deposit in the Himalayan leucogranite belt is a representative hydrothermal deposit. The role of fluid exsolution directly from magma and the fluid reaction with surrounding rocks for ore-forming element enrichment is still controversial. Tourmaline is a significant B-bearing mineral in the hydrothermal deposit, and its geochemical and B isotopic signatures can record the source and evolution of the ore-forming fluid. Two types of hydrothermal tourmaline in the hydrothermal quartz vein (Tur-1) and skarn (Tur-2) were used in this study. Both Tur-1 and Tur-2 have low X-site occupancy and mainly belong to the alkali group. Tur-1 plots in the schorl field, whereas Tur-2 is largely Mg-rich dravite. The B isotope analyses of Tur-1 have $\delta^{11}B$ values of −13.7 to −13.2‰, whereas Tur-2 has higher $\delta^{11}B$ values of −11.1 to −9.3‰. The distinct contact relationship and geochemical compositions suggest that Tur-1 in the hydrothermal vein was formed from a magmatic-hydrothermal fluid with little influence from surrounding rocks and had a genetic relationship with the Cuonadong leucogranite, whereas Tur-2 in the skarn involved more fluid from surrounding rocks with high $\delta^{11}B$ values and strong metasomatic texture. The higher ore-forming element contents in Tur-2 than those in Tur-1 indicate that the reaction between the magmatic exsolution fluid and the surrounding rock is essential for the enrichment and precipitation of ore-forming elements.

KEYWORDS

tourmaline, water−rock interaction, hydrothermal fluids, boron isotope, Cuonadong Sn−W−Be polymetallic deposit

1 Introduction

The Himalayan leucogranite belt in the India–Asia continental collision orogen develops an important and special rare metal mineralization system (Wang et al., 2017; Wu et al., 2020; Cao et al., 2022). Recently, the Cuonadong Sn−W−Be polymetallic deposit in the Himalayan leucogranite belt was discovered, which is the first discovered rare metal deposit with large-scale prospecting potential in this belt (Li et al., 2017; Cao et al., 2020).
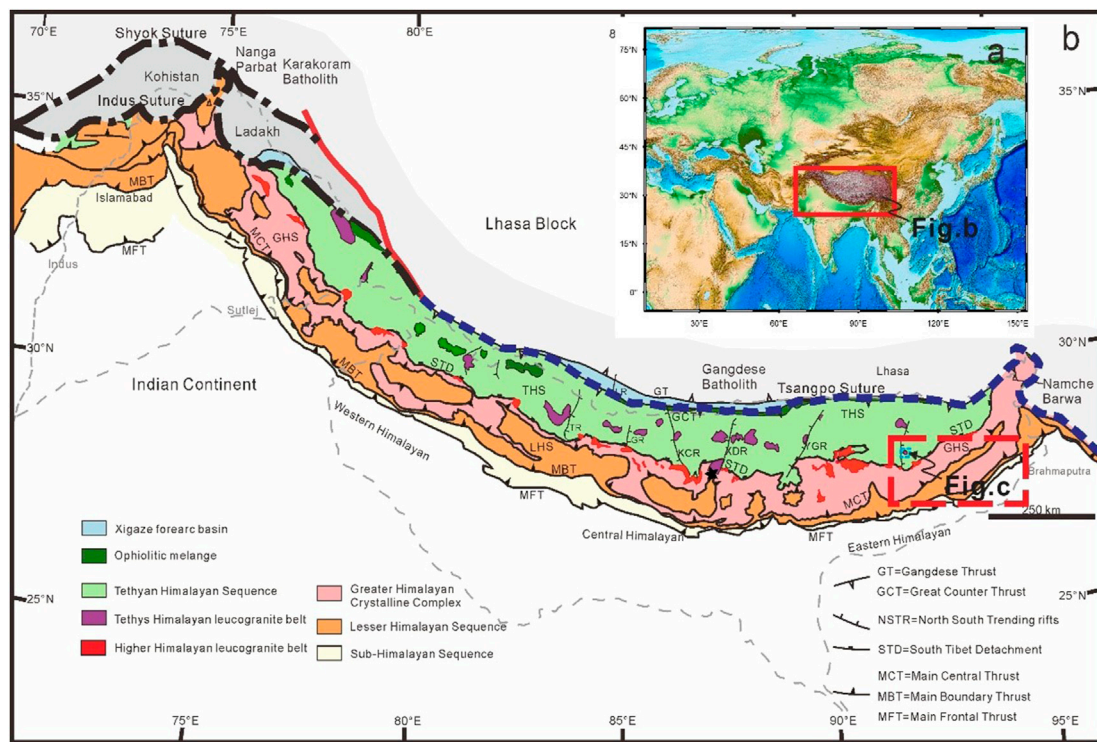
FIGURE 1
Geological map of the Himalayan orogenic belt and Cuonadong dome. **(A)** Map of the Tibetan Plateau. Background relief maps were downloaded from NOAA (https://www.ngdc.noaa.gov/). **(B)** Geological map of the Himalayan orogenic belt (Burg and Bouilhol, 2019; Cao et al., 2020). **(C)** Geological map of the Cuonadong dome and the sample location after Cao et al. (2020).

The preliminary drilling exploration of only the W–Sn–Be orebody in the skarn around the mantle of the gneiss dome found that the average grade of WO₃, Sn, and BeO is 0.21%, 0.36%, and 0.08%, respectively, and the their resource quantities are more than

50,000 tons, 80,000 tons, and 170,000 tons, respectively (Li et al., 2017; Cao et al., 2020). Previous detailed studies mainly focused on the regional geological evolution (Zhang et al., 2017; Zhang L. et al., 2018; Fu et al., 2018; Zhang L. et al., 2019), ore
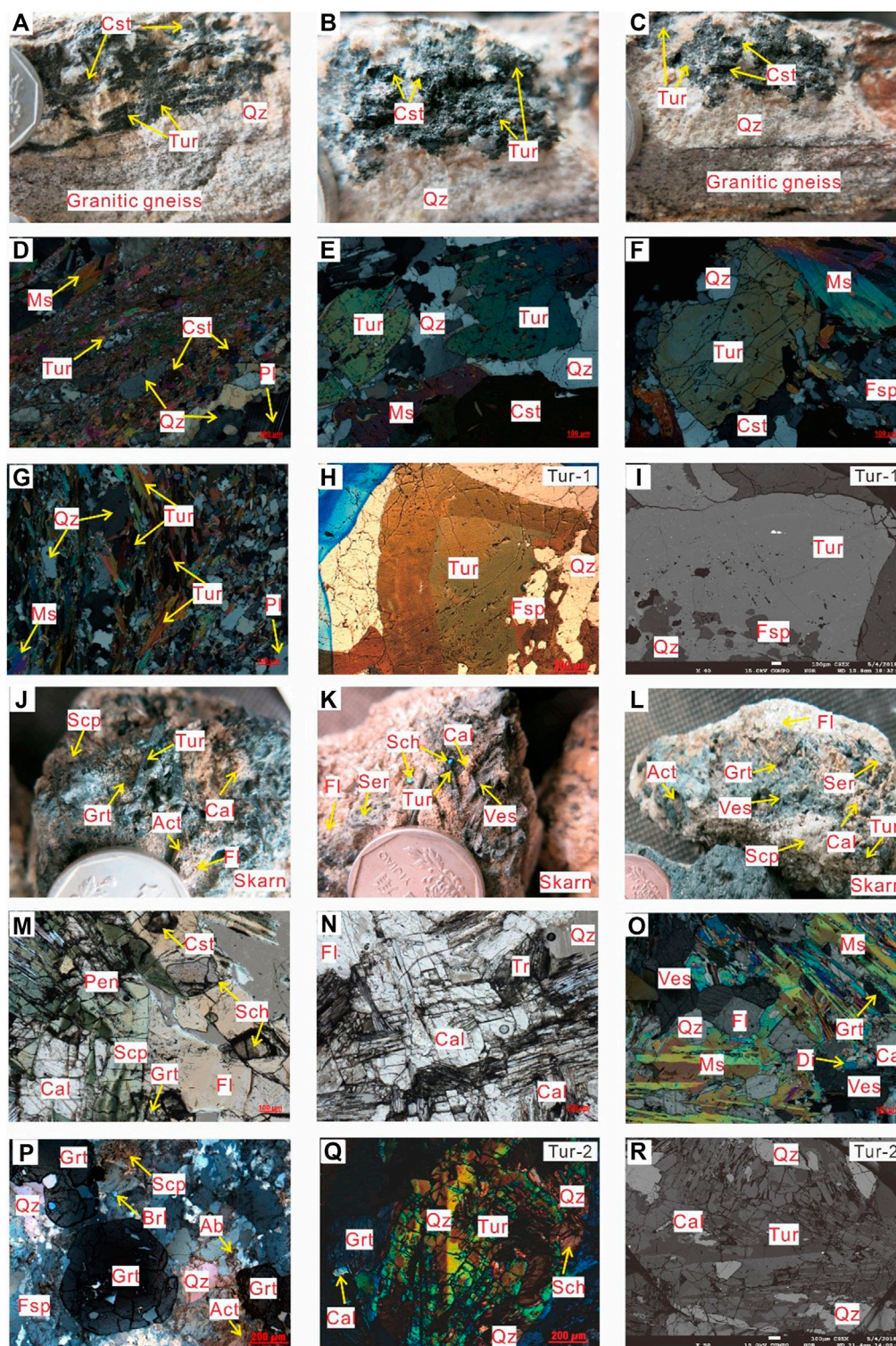
FIGURE 2
Hand specimens, photomicrographs, and backscattered electron images of rocks in the hydrothermal quartz vein **(A−I)** and skarn **(J−R)** from the Cuonadong Sn−W−Be polymetallic deposit. **(A)** Cassiterite-bearing quartz vein, with unconformity of the granitic gneiss. **(B)** Cassiterite-bearing quartz vein with tourmaline, cassiterite, and quartz. **(C)** Cassiterite-bearing quartz vein with unconformity contacting the granitic gneiss. **(D)** Tourmaline, cassiterite, muscovite, plagioclase, and quartz in the hydrothermal quartz vein. **(E)** Tourmaline, cassiterite, muscovite, plagioclase, and quartz in the hydrothermal quartz vein. **(F)** Tourmaline, cassiterite, muscovite, feldspar, and quartz in the cassiterite-bearing quartz vein. **(G)** Tourmaline, muscovite, plagioclase, and quartz in the cassiterite-bearing quartz vein. **(H−I)** Tourmaline in the cassiterite-bearing quartz vein (Tur-1) with a subhedral structure and mineral inclusions in the photomicrograph and backscattered electron image. **(J)** Scapolite, calcite, garnet, fluorite, actinolite, and tourmaline in the skarn. **(K)** Scheelite, tourmaline, sericite, fluorite, calcite, and vesuvianite in the skarn under ultraviolet light. **(L)** Scapolite, tourmaline, sericite, fluorite, calcite, actinolite, and vesuvianite in skarn. **(M)** Calcite, garnet, fluorite, penninite, scheelite, scapolite, and cassiterite in the skarn. **(N)** Calcite, fluorite, tremolite, and quartz in the skarn. **(O)** Calcite, garnet, fluorite, vesuvianite, diopside, quartz, and muscovite in the skarn. **(P)** Garnet, feldspar, scapolite, actinolite, albite, quartz, and beryl in
(Continued)

geology (Li et al., 2017; Cao et al., 2020; Cao et al., 2021), petrology (Huang et al., 2018; Xie et al., 2018; Xia et al., 2019a; Xie et al., 2020; Cao et al., 2022), geochronology (Dong et al., 2017; Xie et al., 2018; Xia et al., 2019a; Xie et al., 2020), mineralogy (Dai et al., 2019; Han et al., 2020; Xie et al., 2020; Dai et al., 2022; Wang et al., 2022; Xie et al., 2022), and evolution of the related leucogranitic magma (Xie et al., 2020; Cao et al., 2022; Xie et al., 2022). However, the hydrothermal activities for the minerogenetic region are complex, and the understanding of the source and evolution of ore-forming fluids for the orebody is still limited.

The hydrothermal orebody is widely hosted in metamorphic surrounding rocks, including the hydrothermal vein-type Sn–W–Be orebody faulted by north–south-trending rifts and the skarn-type W–Sn–Be orebody in the strongly deformed mantle of the gneiss dome (Cao et al., 2020; Cao et al., 2021; Dai et al., 2022; Wang et al., 2022). Both hydrothermal vein-type and skarn-type orebodies experienced extensive hydrothermal alteration induced by ore-forming fluids (Cao et al., 2020; Cao et al., 2021; Cao et al., 2022; Dai et al., 2022; Wang et al., 2022). The mineralization process in the Cuonadong Sn–W–Be polymetallic deposit is not fully understood. Previous studies have suggested that the direct fluid exsolution from magma and the fluid reaction with surrounding rocks are the two key processes of ore-forming element enrichment (Audtat et al., 2000; Schmidt, 2018; Dai et al., 2022). Here, we aimed at providing new clues for deciphering the enrichment process of ore-forming elements in the Cuonadong Sn–W–Be polymetallic deposit.

Tourmaline is the main boron-bearing mineral in hydrothermal ore deposits formed in different geological settings (Hazarika et al., 2019; Zheng et al., 2019; Daver et al., 2020; Harlaux et al., 2020; Trumbull et al., 2020). Meanwhile, tourmaline has stable physicochemical properties and a negligible element diffusion rate (van Hinsberg et al., 2011a; van Hinsberg et al., 2011b). Importantly, continental crust and most clastic metasediments have relatively low Ca contents and negative $\delta^{11}B$ values (Rudnick and Gao, 2003; Trumbull and Slack, 2018), whereas marble and marine carbonate usually contain high Ca contents and positive $\delta^{11}B$ values (Melezhik et al., 2005; Marschall and Jiang, 2011). Thus, the tourmalines derived from different sources show significantly different element and boron isotope compositions (Harlaux et al., 2020; Trumbull et al., 2020; Pei et al., 2023). This makes tourmaline an excellent messenger for tracing the origin of fluids (Marschall and Jiang, 2011; Harlaux et al., 2020; Trumbull et al., 2020; Chakraborty, 2021). With the development of *in situ* analytical techniques, the element and B isotope compositions of tourmalines have been widely used to decipher hydrothermal evolution and mineralization processes in recent years (Trumbull et al., 2018; Zhang W. et al., 2018; Zhao et al., 2019; Harlaux et al., 2020).

In the Cuonadong Sn–W–Be polymetallic deposit, tourmaline has a close spatial and temporal relationship with cassiterite and scheelite formed during the late retrograde skarn and hydrothermal quartz vein stages (Cao et al., 2021; Dai et al., 2022; Wang et al., 2022), which can

be an excellent indicator to study the source and evolution of ore-forming fluids. In this study, we analyze the *in situ* major and trace element and boron isotope compositions of tourmalines hosted in the hydrothermal quartz vein and the skarn from the Cuonadong Sn–W–Be polymetallic deposit to define the source of the hydrothermal fluid and the role of the surrounding rock.

2 Geological background and samples

2.1 Regional geological background

The Qinghai–Tibetan Plateau, situated in western China, has experienced the tectonic evolution of subduction and continental collision (Yin and Harrison, 2000; Pan et al., 2012). It consists of five parallel E-W trending blocks from north to south, including the Songpan–Ganzi, the north and south Qiangtang, Lhasa, and Himalayan blocks (Yin and Harrison, 2000; Yin, 2006; Pan et al., 2012). The Himalayan orogeny is the Cenozoic large-scale continent collision orogeny between the Indian Craton and Lhasa blocks (55 ± 10 Ma) on the Himalaya block, following the closure of the Neo-Tethys Ocean (Hu et al., 2016; Najman et al., 2017; Zheng and Wu, 2018) (Figures 1A,B). This orogeny is separated from the Lhasa block by the Indus–Yarlung Tsangpo Suture Zone and from the Indian Craton by the Main Frontal Thrust (Yin, 2006). Four geologic domains along the Himalayan orogeny are divided by the South Tibetan detachment system, the Main Central Thrust, and the Main Boundary Thrust from south to north, which are named as the sub-Himalaya, the Lower Himalayan sequence, the Higher Himalayan sequence (HHS), and the Tethyan Himalayan sequence (THS) (Yin, 2006). The sub-Himalayan sequence and the Lower Himalayan sequence are composed of the Neogene fluvial sediments and Proterozoic greenschist–amphibolite facies metasedimentary rocks (Kohn, 2014; Goscombe et al., 2018; Mukherjee et al., 2019). The HHS is composed of crystalline complexes with Late Proterozoic to Early Paleozoic greenschist to granulite–eclogite facies metamorphic rocks (Kohn, 2014; Mukherjee et al., 2019). The THS is sandwiched between the HHS and the Lhasa terrane and comprised Paleozoic to Paleogene low-grade metamorphic clastic and carbonate rocks and magmatic rocks (Cao et al., 2018). The Oligocene–Miocene Himalayan leucogranite (45–7 Ma) was formed by the continental crust thickening and remelting during the evolution of Himalayan orogeny and is widely emplaced and distributed in the HHS and THS (Wu et al., 2015; Wu et al., 2020). These leucogranites can be divided into two sub-parallel and EW-trending magmatic rock belts, namely, the Higher and the Tethyan Himalayan leucogranite belts (Wu et al., 2015; Wu et al., 2020). It is noteworthy that a series of gneiss domes occurring in the THS constitute the discontinuous beaded North Himalayan gneiss domes, which is a typical feature of the Tethyan Himalayan

orogenic belt (Cao et al., 2020; Wu et al., 2020). These domes were intruded by the Oligocene–Miocene leucogranites, which are typically covered in high-grade metamorphic facies Early–Middle Paleozoic and Neoproterozoic granitic gneisses (Zhang L. et al., 2019; Zhang L. K. et al., 2019). As the highly differentiated and strong peraluminous characteristics of the leucogranites in the dome, many rare metal minerals have been found, like scheelite, cassiterite, and beryl, in the granitic magmatic-hydrothermal system, which confirmed the great metallogenic potential in and around the Himalayan domes (Wang et al., 2017). The preliminary studies of the Cuonadong Sn–W–Be deposit in the Cuonadong dome confirmed the gneiss dome in the THS has great metallogenic potential of rare metals (Li et al., 2017; Dai et al., 2022; Wang et al., 2022).

2.2 Geology of the Cuonadong dome

The Cuonadong dome, covering an area of 400 km^2, is a typical gneiss dome located in the southeastern Tethyan Himalayan leucogranite belt (Li et al., 2017; Zhang et al., 2017). The dome is mainly controlled by the South Tibetan Detachment System and NS-trending rifts (NSTRs) (Dong et al., 2017; Fu et al., 2018; Xie et al., 2018; Cao et al., 2020) (Figure 1C). Based on the upper brittle detachment fault and the lower brittle-ductile slip fault, the Cuonadong dome can be divided into three parts from inside to outside (Zhang L. et al., 2018; Huang et al., 2018; Xie et al., 2018; Cao et al., 2020; Xie et al., 2020). The circum of the dome is covered by the Triassic–Jurassic metasedimentary and sedimentary rocks. The core and mantle parts of the dome consist of the Cambrian orthogneisses and the Miocene leucogranitic rocks, surrounded by strongly deformed Paleozoic metamorphic quartz schist interlaced with marble (Zhang L. et al., 2018; Cao et al., 2020; Dai et al., 2022). The granitic dykes are widespread and intercalated into the surrounding rocks, accompanied by extensive hydrothermal polymetallic mineralization (Wang et al., 2017; Liang et al., 2018; Cao et al., 2021; Dai et al., 2022; Wang et al., 2022).

2.3 Geology of the ore deposit

The Cuonadong Sn–W–Be polymetallic deposit is situated in the Cuonadong dome and mainly enriched in Sn, W, and Be (Cao et al., 2020; Cao et al., 2021; Dai et al., 2022; Wang et al., 2022). Mineralization is widely distributed in the Cuonadong dome with large inferred SnO_2, WO_3, and BeO resources. There are four regions with significant metallogenic potential, namely, Xianglin, Dongjie, Rina, and Changming (Cao et al., 2020; Cao et al., 2021; Dai et al., 2022) (Figure 1C). The Xianglin area in the northwestern part of Cuonadong has the largest inferred resources, and the hydrothermal vein-type Sn–W–Be mineralization and skarn-type W–Sn–Be mineralization have been delineated (Li et al., 2017; Cao et al., 2021; Dai et al., 2022; Wang et al., 2022). Thus, the hydrothermal mineralization types in the Xianglin area have been represented as the key research area in this study.

1) Hydrothermal vein-type Sn–W–Be orebody in the Xianglin area. There were north–south trending faults and detached faults in the Xianglin area, which cut the deformed granitic gneiss and schist strata (Figures 2A–C). The fracture zone formed the breccia with a width of >0.3 m. With the hydrothermal elevation from the leucogranite outward to the surrounding rock, the hydrothermal cassiterite-bearing quartz veins, cassiterite–sulfide veins, and fluorite–quartz veins were cemented in the fracture zone. The formation of those hydrothermal veins can be divided into three stages: in the first stage, the cassiterite-bearing quartz vein was composed of cassiterite, quartz, plagioclase, tourmaline, and muscovite; in the second stage, the cassiterite–sulfide vein contained cassiterite, quartz, chalcopyrite, arsenopyrite, sericite, and fluorite; and in the third stage, fluorite–quartz veins consisted of fluorite, quartz, and calcite with little mineralization (Cao et al., 2021; Wang et al., 2022). The hydrothermal vein-type Sn–W–Be orebody was mainly formed in the cassiterite-bearing quartz vein. The mineral associations in the cassiterite-bearing quartz vein include cassiterite, scheelite, muscovite, quartz, fluorite, and tourmaline (Figures 2D–I). The tourmaline from the first mineralization stage in the cassiterite-bearing quartz vein is selected in this study, which can represent the initial composition of hydrothermal evolution.

2) Skarn-type W–Sn–Be orebody in the Xianglin area. The number of early Paleozoic marble stratum is distributed in the mantle of the Cuonadong dome, and their thickness is up to 20–300 m. The Miocene undeformed leucogranite and pegmatite dikes extensively touched and invaded the marble, resulting in intense skarnization in the contact zone with widths of 1–20 m. Skarnization promoted the W–Sn–Be enrichment in the skarn and formed the skarn-type orebodies with lenticular and cystic structures (Cao et al., 2020; Cao et al., 2021). The metasomatic texture of the skarn-type ore is obvious (Figure 2J–L). The main ore minerals in skarn-type mineralization are scheelite, cassiterite, and beryl, accompanied by secondary metallic minerals, such as arsenopyrite, magnetite, and pyrite. The non-metallic minerals are tourmaline, quartz, feldspar, muscovite, fluorite, garnet, chlorite, scapolite, actinolite, penninite, vesuvianite, calcite, albite, tremolite, and diopside (Figures 2M–R). The size of mineral crystals can reach more than 1 cm. During skarnization, the early prograde skarn minerals, including garnet, diopside, vesuvianite, scapolite, and minor fluorite, were extensively leached and replaced by late retrograde skarn minerals (Cao et al., 2020), including tremolite, quartz, feldspar, actinolite, fluorite, scheelite, cassiterite, calcite, and tourmaline (Figures 2M–R).

2.4 Tourmaline samples

In this study, tourmalines from the hydrothermal vein (Tur-1) and skarn (Tur-2), which coexist with cassiterite, scheelite, beryl, and gangue minerals, are collected for in situ geochemical composition analyses.

2.4.1 Tourmaline in the hydrothermal quartz vein (Tur-1)

The sample CND-42 was collected from a cassiterite-bearing hydrothermal quartz vein in the Cuonadong dome (Figures 2A–C). This hydrothermal vein sample is clearly separated from the surrounding granitic gneiss by a dark reaction belt. The hydrothermal vein contains tourmaline aggregates, accounting for approximately 20% of the total volume. They

also have quartz and feldspar contents of 60% and muscovite content of 10%. The contents of cassiterite and scheelite are about 5%. There is a small amount of accessory minerals like zircon and apatite.

Tourmalines from the hydrothermal vein (Tur-1) are mostly acicular, columnar, and bulk aggregates. The tourmaline nucleus is blue–green, and the boundary is dark brown under single polarized light (Figures 2D–H), and they have no zonation under the BSE image (Figure 2I). These tourmalines are subhedral and contain muscovite, feldspar, and quartz particles (Figures 2H,I). At the same time, some tourmalines cutting quartz, feldspar, and muscovite are evident in hand specimens and microscopic photographs (Figures 2B,F). The mineralogical relationships between tourmaline and other minerals mean that Tur-1 was formed in the late crystal sequence compared to muscovite, feldspar, and quartz.

2.4.2 Tourmaline in skarn (Tur-2)

The skarn sample CND-24 was collected near the Xianglin area of the Cuonadong dome undergoing mineralization (Figure 1C). The volume content of tourmaline exceeds 20%. The voids between tourmaline grains are generally filled with fluorite, calcite, K-feldspar, muscovite, cassiterite, and scheelite (Figure 2J–L).

Tourmaline gains in the skarn (Tur-2) are subhedral–anhedral crystals with cataclastic or fibrous texture, showing strong pleochroism from yellow to blue and lacking optical zoning (Figure 2Q). In the BSE image, tourmaline also has no zonation (Figure 2R). Meanwhile, calcite and quartz are symbiotic and were included in the tourmaline.

3 Analytical methods

In this study, all samples were first polished in thin sections and were carbon-coated to investigate growth zonation using a scanning electron microscope (SEM) prior to further analyses. Backscattered electron (BSE) images were collected on a scanning electron microscope at the Testing Center of Shandong Bureau, China Metallurgical Geology Bureau (Jinan). Based on BSE imaging, we selected the representative sites of tourmaline

grains for *in situ* major and trace element content and B isotope composition analyses using an electron microprobe and by LA-(MC)-ICP-MS.

3.1 Electron microprobe analysis

Major element compositions of tourmaline were analyzed at the Testing Center of Shandong Bureau, China Metallurgical Geology Bureau (Jinan), using a JEOL JXA- 8230 electron probe microanalyzer (EPMA). The boost voltage is 15 kV, and the beam current is 20×10^{-8} A. All values in which the total amount is less than 95% are eliminated. The integral times of the peak value and background value are 10 s and 5 s, respectively. Feldspar (Al-Kα and K-Kα), rhodonite (Ca-Kα and Si-Kα), forsterite (Mg-Kα), rutile (Ti-Kα), chromite (Cr-Kα), and hematite (Fe-Kα) were used for calibration as the natural and synthetic internal mineral standards.

3.2 LA-(MC)-ICP-MS analysis

Trace element analyses of tourmaline were performed by LA-ICP-MS at the CAS Key Laboratory of Mineralogy and Metallogeny, Guangzhou Institute of Geochemistry, Chinese Academy of Sciences. *In situ* trace element analyses of tourmaline were obtained on polished thin sections using a Resonetics RESOlution S-155 ArF-Excimer laser source (λ = 193 nm) coupled with an Agilent 7900 ICP-MS instrument. The NIST SRM 610, the USGS glasses, and GOR132-G were repeatedly analyzed between every eight points during the analyses. Both standards and samples were ablated using a 43-μm spot size, energy density of 3.24 J/cm^2, and 6-Hz repetition rate, and the residence time for every point is 20 s.

Tourmaline B isotope compositions were measured by LA-(MC)-ICP-MS at the State Key Laboratory of Geological Processes and Mineral Resources at the China University of Geosciences (Wuhan). Tourmaline B isotope analyses were obtained using a Nu plasma II multi-collector coupled with a RESOlution S-155 laser ablation system. Analyses were carried out with a beam diameter of 50 μm, energy density of 5 J/cm^2, and 10-Hz repetition rate. Previous studies have provided detailed analytical
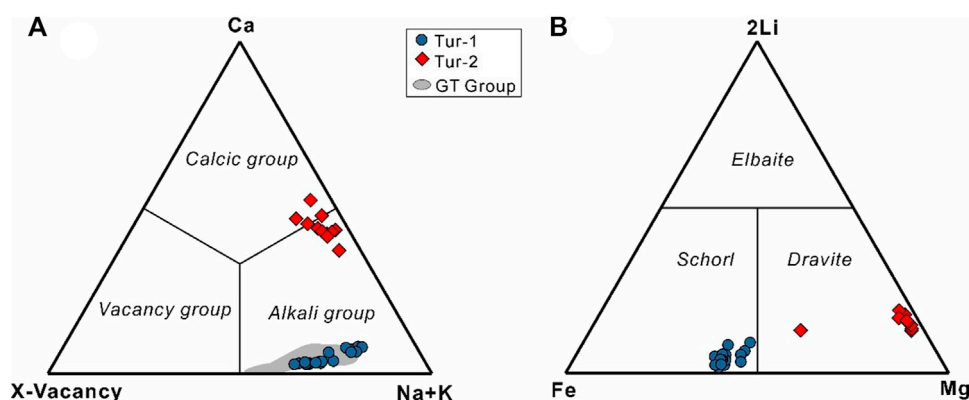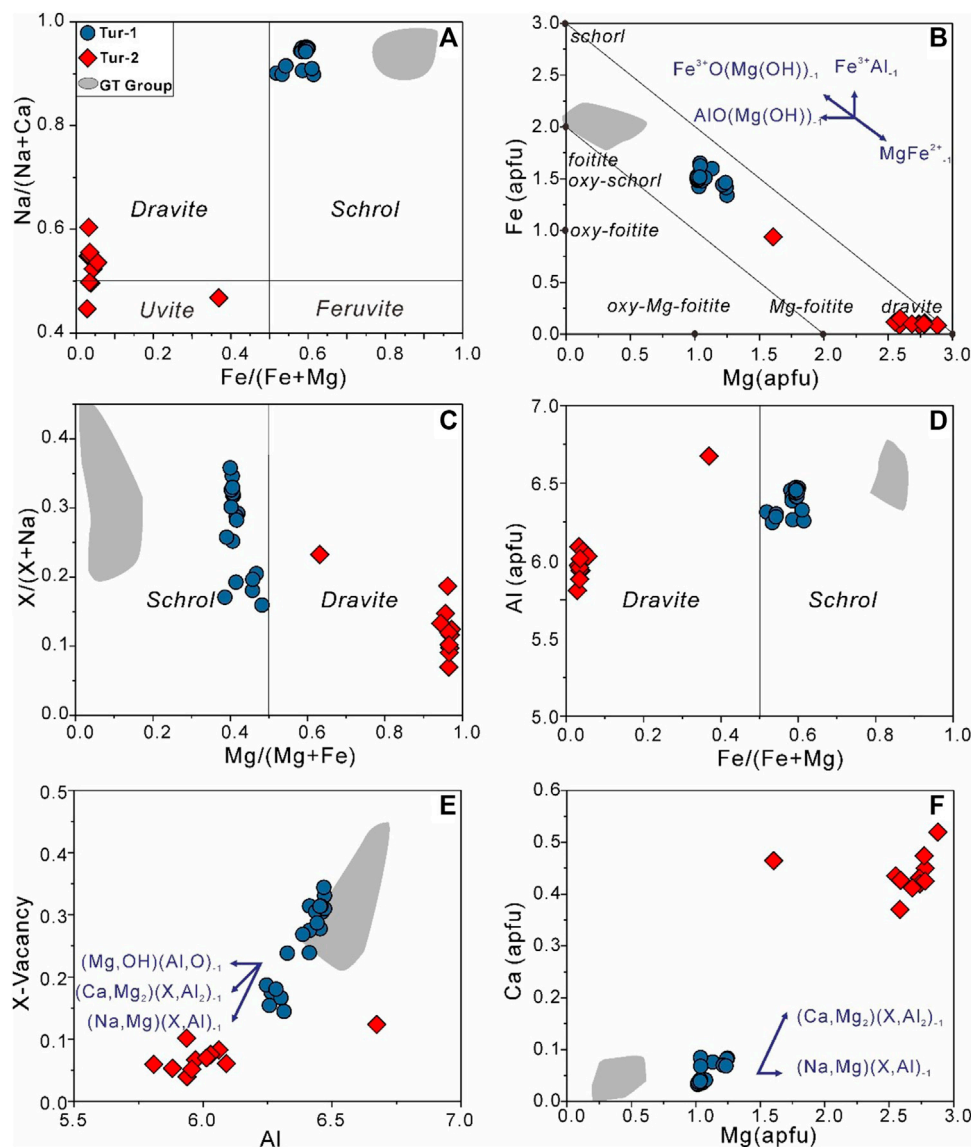

FIGURE 3
Classification of the principal groups of hydrothermal tourmaline Tur-1 and Tur-2 from the Cuonadong Sn−W−Be polymetallic deposit. The Ca-X-vacancy-Na+K **(A)** and 2 Li-Fe-Mg **(B)** ternary diagrams are obtained from Henry et al. (2011). The tourmaline data in the Cuonadong leucogranite from the Xinglin area (GT group, gray area) were obtained from Xie et al. (2022).

FIGURE 4
Diagrams for Tur-1 and Tur-2 in the hydrothermal vein and skarn from the Cuonadong Sn−W−Be polymetallic deposit, showing the chemical compositional evolution and classification of hydrothermal tourmaline. **(A−D)** Classification diagrams for tourmaline species; **(E−F)** plot of Al *versus* X-site vacancies and Mg *versus* Ca. The tourmaline data in the leucogranite in the Xianglin area in the Cuonadong dome (GT group, gray area) were obtained from Xie et al. (2022).

procedures (Hou et al., 2010; Yang et al., 2015a; Yang et al., 2015b; Zhao et al., 2019). In this study, the repeated analysis of the reference tourmaline sample IMR RB1 from Hou et al. (2010) is expected to be more accurate than 0.8‰, with a test value of −13.1‰ ± 0.7‰.

4 Results

The selected Tur-1 and Tur-2 are subhedral and widely distributed in hydrothermal veins and skarns. In this study, the tourmalines show clear inclusions in the polarizing microscope and BSE images. The inclusions generally contain quartz, feldspar, muscovite, calcite, and other minerals, which indicates that tourmaline was crystallized in the hydrothermal stage. The major and trace element results and B isotope compositions of Tur-1 and Tur-2 are given in Supplementary Table 1.

4.1 Major elements in the hydrothermal tourmaline

The tourmaline structural formulae were obtained by assuming a general formula with 15 cation numbers in $(Y + Z + T)$ sites and 31 anions in the crystal (Henry et al., 2011) and based on $B = 3$ and $OH + F + Cl = 4$ in the molecular formula to obtain the B_2O_3 and H_2O contents, respectively (Henry et al., 2011; Henry and Dutrow, 2018). Based on tourmaline compositions, Tur-1 belongs to the alkali group, schorl. Meanwhile, more than half the portion of the Tur-2 samples plot in the field of alkali group and dravite, whereas a small portion of Tur-2 belongs to the calcic group and dravite (Figure 3; Figures 4A−D).

Tur-1 and Tur-2 from the hydrothermal vein and skarn show considerable differences in CaO, MgO, FeO, and Na_2O compositions (Figure 4). Compared to Tur-1, Tur-2 contains distinctly higher Ca and
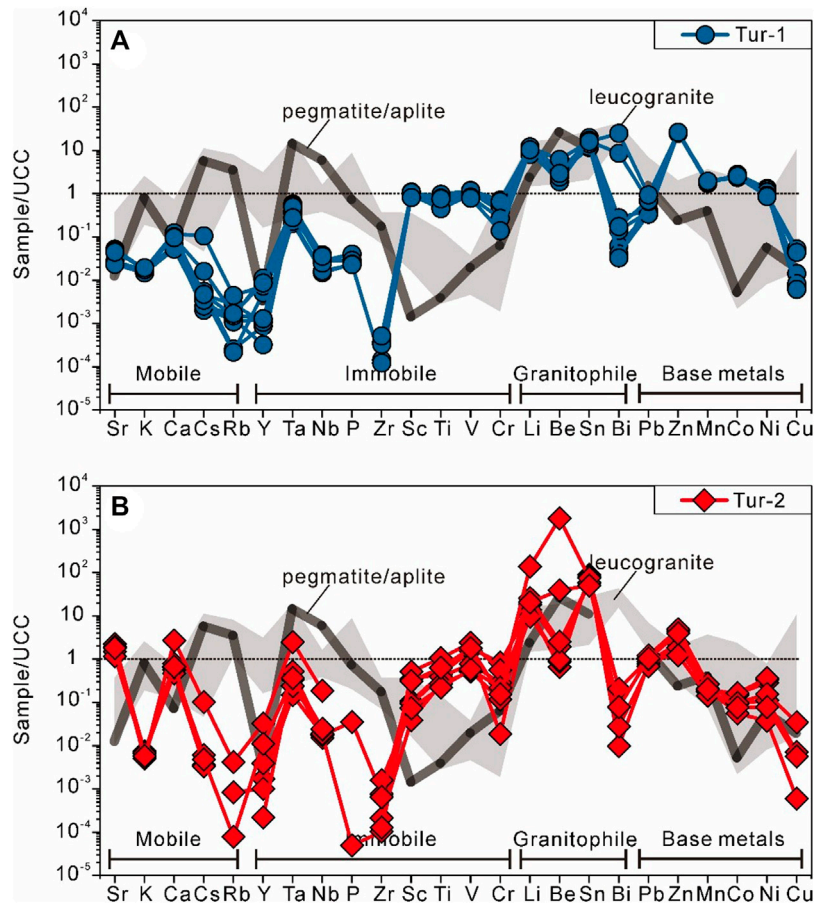
FIGURE 5
Upper continental crust-normalized spider diagram of Tur-1 and Tur-2 from the Cuonadong polymetallic deposit. The upper continental crust data and the classification of trace elements are from Rudnick and Gao (2003) and Decrée et al. (2013). The whole-rock major and trace element data on Cuonadong leucogranite and pegmatite/aplite in the Xianglin area are from Huang et al. (2018), Xie et al. (2018), Xia et al. (2019a), and Xie et al. (2020). **(A)** Upper continental crust-normalized spider diagram of Tur-1 is shown as blue circle and line. **(B)** Upper continental crust-normalized spider diagram of Tur-2 is shown as red rhombus and line.

Mg contents and lower Fe and Na contents. The Tur-2 data plot in the dravite field or between the dravite and uvite fields, with Mg/(Mg + Fe) of 0.40–0.96 and Na/(Na + Ca) of 0.12–0.60. Meanwhile, Tur-1 is Fe-rich and plots in the schorl field, with Mg/(Mg + Fe) of 0.38–0.48 and Na/(Na + Ca) of 0.89–0.95 (Figure 4). For Tur-1, the variation of Al and Mg is consistent with a general inverse correlation between X-site vacancy and Ca, implying some Al^{3+} and Mg^{2+} substitutions in accordance with the $(Na, Mg) (X, Al)_{-1}/(Ca, Mg_2) (X, Al_2)_{-1}$ exchange vector (Henry et al., 2011; Henry and Dutrow, 2018; Xie et al., 2022) (Figures 4E,F). The variation of Ca and Mg contents in Tur-2 could be controlled by the $(Ca, Mg_2) (X, Al_2)_{-1}/AlO(Mg(OH))_{-1}$ exchange vector (Yang et al., 2015b; Dutrow and Henry, 2018; Henry and Dutrow, 2018; Harlaux et al., 2020; Zhao et al., 2022) (Figures 4E,F).

4.2 Trace elements in the hydrothermal tourmaline

Tur-1 has lower Sn and Sr contents but higher Zn contents than Tur-2 (Figures 5, 6). All the hydrothermal tourmalines show relatively similar Nb/Ta ratios (Figure 6). Meanwhile, these element contents of Tur-1 tourmalines show overlapping ranges with those of Tur-2 and extend to

lower Li, Be, Ba, Pb, and REE contents and Eu/Eu* values (Figure 6). In addition, all types of tourmalines have negligible Gd, Tb, Dy, Ho, Tm, Yb, Lu, Hf, W, and U contents, which are below the detection limits.

Both tourmalines are enriched in light rare earth elements (LREEs) and extremely depleted in heavy rare earth elements (HREEs) with positive Eu anomalies, displaying a right-inclined pattern (Figure 7). However, Tur-1 has a larger range of REE contents and higher LREE contents than Tur-2 (Figures 6, 7).

4.3 Boron isotope compositions in the hydrothermal tourmaline

The boron isotope results have a difference between Tur-1 and Tur-2. Tur-1 has relatively homogeneous $\delta^{11}B$ values of −13.7 to −13.2‰ (an average of −13.5‰), whereas Tur-2 has higher $\delta^{11}B$ values (−11.1 to −9.3‰, an average of −10.6‰) (Figure 8). In addition, the $\delta^{11}B$ values of the tourmaline grains in this study from the core to the rim are similar (Figure 9). Compared to the hydrothermal tourmalines in this study, magmatic tourmalines from the leucogranite (GT Group) in the Xianglin area in the Cuonadong dome have $\delta^{11}B$ values ranging from −8.7 to −8.0‰ (an average of −8.3‰) (Xie et al., 2022) (Figures 8, 9).

FIGURE 6
Correlation diagrams between trace elements or ratios and Mg/(Mg + Fe) in the tourmaline from the Cuonadong leucogranite (GT group, gray square), hydrothermal quartz vein (Tur-1, blue circle), and skarn (Tur-2, red rhombus) in the Cuonadong Sn−W−Be polymetallic deposit. **(A)** Li vs. Mg/(Mg + Fe); **(B)** Be vs. Mg/(Mg + Fe); **(C)** Sn vs. Mg/(Mg + Fe); **(D)** Zn vs. Mg/(Mg + Fe); **(E)** Ba vs Mg/(Mg + Fe); **(F)** Pb vs. Mg/(Mg + Fe); **(G)** Nb/Ta vs. Mg/(Mg + Fe); **(H)** Sr vs. CaO; **(I)** Eu/Eu* vs REE. The data on the tourmaline from the Cuonadong leucogranite in the Xianglin area (GT group, gray square) are obtained from Xie et al. (2022).
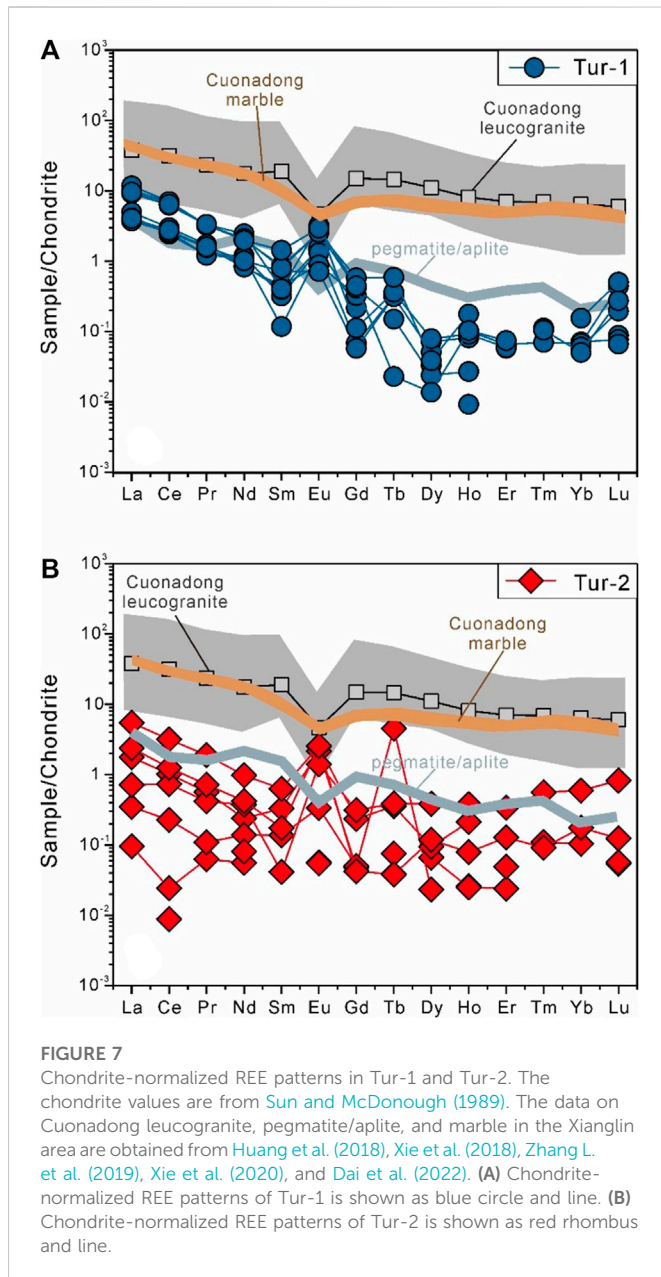
5 Discussion

5.1 Origin of tourmalines in the hydrothermal vein and skarn

Geochemical and mineralogical characteristics are usually used to indicate the genesis and crystallization sequence of minerals (Pirajno and Smithies, 1992; Siahcheshm et al., 2014; Rezaei Azizi et al., 2018a; Rezaei Azizi et al., 2018b; Rajabpour et al., 2018; Zhao et al., 2019; Abedini et al., 2020; Harlaux et al., 2020). In the Mg-Fe/(Fe + Mg) diagram, the Fe/(Fe + Mg) values of tourmaline indicate their distance from the granitic source in a granite-related hydrothermal Sn−W deposit (Pirajno and Smithies, 1992). All of the tourmalines in this study plot in the distal area (<0.6), which illustrates that tourmaline-forming hydrothermal fluids may have traveled a considerable distance from their source (Figure 10). Harlaux et al. (2020) proposed that hydrothermal tourmalines have lower Li/Sr values (<30) than the magmatic tourmalines. The tourmalines in this

study exhibit low Li/Sr values of 14.9–24.2 (Tur-1) and 0.33–4.70 (Tur-2), which indicate that the tourmalines in this study are all hydrothermal tourmalines.

Tur-1 in the cassiterite-bearing quartz vein was homogeneous (like the Mg/(Mg + Fe) value) without the oscillating growth zone in the BSE (Figure 9). Moreover, Tur-1 was intergrown with/including other minerals (e.g., quartz and feldspar) with planar or arc-shaped contacts. All the characteristics mean that Tur-1 crystallized later than quartz and feldspar during the hydrothermal evolution and is primary hydrothermal tourmaline. Tur-1 in the hydrothermal vein along north–south-trending faults and detached faults in the Xianglin area generally occurs in the surrounding rock matrix and cassiterite-bearing quartz vein rims and has textures parallel to the fault (Cao et al., 2020; Wang et al., 2022). This texture suggests the formation and existence of detached faults caused the expulsion of accumulating hydrothermal fluids from the magma along the faults into the surrounding granitic gneiss. With hydrothermal fluid invasion, it has been observed that the partial major element

FIGURE 7
Chondrite-normalized REE patterns in Tur-1 and Tur-2. The chondrite values are from Sun and McDonough (1989). The data on Cuonadong leucogranite, pegmatite/aplite, and marble in the Xianglin area are obtained from Huang et al. (2018), Xie et al. (2018), Zhang L. et al. (2019), Xie et al. (2020), and Dai et al. (2022). **(A)** Chondrite-normalized REE patterns of Tur-1 is shown as blue circle and line. **(B)** Chondrite-normalized REE patterns of Tur-2 is shown as red rhombus and line.

compositions of hydrothermal tourmaline may be influenced by the surrounding rock composition depending on the water–rock ratio (Yang et al., 2015b; Zhang W. et al., 2018). Tur-1 displays semblable Al, Ca, and Na + K contents with magmatic tourmalines in the leucogranite from Xie et al. (2022) (Figure 4). Tur-1 has different geochemical compositions with higher Mg/(Mg + Fe) (0.39–0.48) and lower Ca values (0.18–0.46 wt%) and Na/(Na + Ca) values (0.91–0.96) than the surrounding granitic gneiss (Mg/(Mg + Fe): 0.05–0.08; Ca: 0.92–1.22 wt%; and Na/(Na + Ca): 0.82–0.85) from Xia et al. (2019b), which show that the granitic gneiss was less mixed into the magmatic-hydrothermal fluid from the geochemical perspective. This feature is similar to the hydrothermal tourmaline in Yang et al. (2015b). Thus, geochemical evidence attests that Tur-1 growth was mainly inherited from the composition of the original magmatic-hydrothermal fluid. However, feldspar grains in the matrix of the surrounding rock show the feature of hydrothermal alteration (Wang et al., 2022), suggesting the existence of a water–rock reaction between the hydrothermal fluid

and surrounding rock, while the observation of hand specimens (Figure 2A) reveals a weak water–rock reaction. This is also supported by that hydrothermal minerals such as tourmaline and sericite only occur in the veins. This phenomenon is also discovered in the hydrothermal tourmalines in other deposits (Yang and Jiang, 2012; Yang et al., 2015a; Zhang W. et al., 2018). In summary, both the geochemical composition and mineral texture show Tur-1 was mainly formed from magmatic-hydrothermal fluids with limited influence of water–rock reaction (Figure 8).

Tur-2 in the skarn, represented as euhedral grains containing quartz and sericite inclusions, has an arresting metasomatic texture (Figure 2D) and high Mg and Ca contents (Figure 4). This may be attributed to the dissolution of Mg- and Ca-rich minerals, such as calcite and dolomite, from the surrounding marble during the skarnization process. In addition, Tur-2 exhibits pleochroism and fibrous texture, which is proved to be typically formed in a multistage hydrothermal fluid environment with relatively low temperatures (<500 °C) during water–rock interactions (Dutrow and Henry, 2016; Zhao et al., 2019). The aforementioned features suggest that the fluid responsible for Tur-2 should have a disparate composition and a low temperature, which is consistent with the reported low hydrothermal temperatures (250°C–380°C) for fluid inclusions in the skarn (Dai et al., 2022). Such geochemical and textural characteristics suggest that Tur-2 was mainly formed by a metasomatism process during skarnization with extensive water–rock reactions.

5.2 Source and evolution of hydrothermal fluid

### 5.2.1 Major trace element tracing magmatic-hydrothermal processes

The crystallization sequence of tourmalines (from the GT group, Tur-1 to Tur-2) is consistent with the compositional variations expected during late-stage boron-rich magma fractionation with the evolution of the magmatic-hydrothermal tourmaline generally following the $MgFe_{-1}$ substitution vector (schorl-dravite) (Figure 4B). The GT group shows high Nb/Ta values, indicating that they were likely crystallized from B-rich melts early immiscible with granitic magmas (Figure 6G). Tur-1 and Tur-2 formed in the B-rich fluids that continuously separated from more evolved granitic magma, supported by their consistently low Nb/Ta values (Figure 6G). Tur-1 has higher Mg/(Mg + Fe) values (Figure 6) than the GT group, consistent with the changes from the Fe-rich magmatic tourmaline to Mg-rich hydrothermal tourmaline, which have been observed in other granite Sn–W metallogenic systems (Zhao et al., 2019; Zheng et al., 2019). Moreover, the extreme enrichment of Sr and CaO contents in Tur-2 confirmed the presence of marble components (Figure 6H).

The trace element concentrations in tourmaline are generally controlled by the composition of the melts and magmatic-hydrothermal fluids from which it crystallized, which caused differences in the same tourmaline in the major trace element compositions (van Hinsberg, 2011; Zhao et al., 2019). The fluctuations of Mg/(Mg + Fe) values and Ba and Pb contents in Tur-2 (Figures 6E,F) reflect the gradual leaching and decomposition processes of the early minerals and marble with the extensive water–rock reactions during late retrograde skarnization. The decrease of Zn from the GT group, Tur-1 to Tur-2 (Figure 6D), may reflect crystallization differentiation of silicates
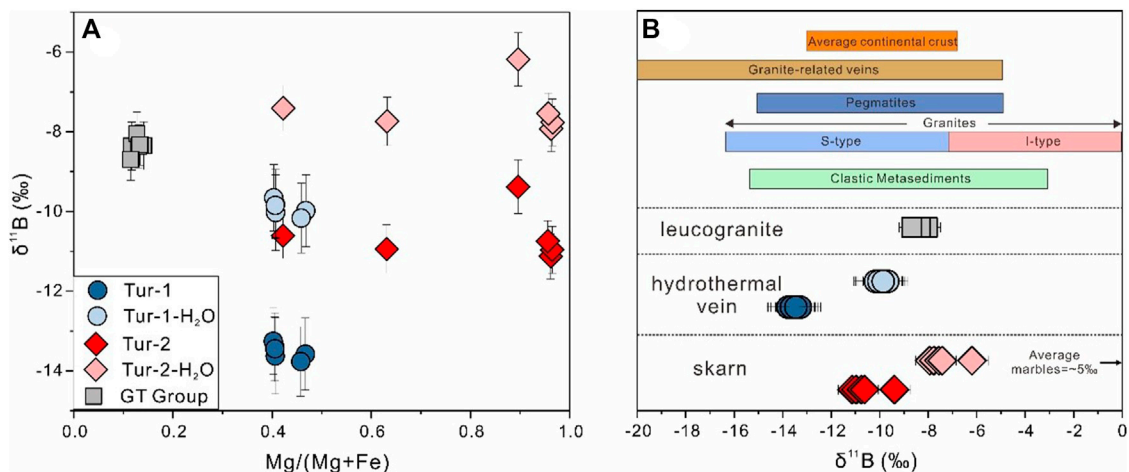
FIGURE 8
Boron isotope variations of Tur-1 and Tur-2. **(A)** δ¹¹B values vs Mg/(Mg + Fe) values. **(B)** Measured B isotope and calculated hydrothermal fluid compositions of Tur-1 and Tur-2 compared with inferred B sources. The tourmaline composition data on leucogranite in the Xianglin area (GT group, gray square) are obtained from Xie et al. (2022). Measured values of B isotope compositions in Tur-1 and Tur-2 are indicated by the blue circle and red rhombus, respectively. The calculated hydrothermal fluids of Tur-1 and Tur-2 are indicated by the light blue circle and light red rhombus, respectively. To compare the composition of the source area, the composition range of tourmaline boron isotopes in various rocks and continental crust around the world is also marked, and the data are collected from Jiang and Palmer (1998), Xavier et al. (2008), Marschall and Jiang (2011), Trumbull and Slack (2018), and Zhou et al. (2019).
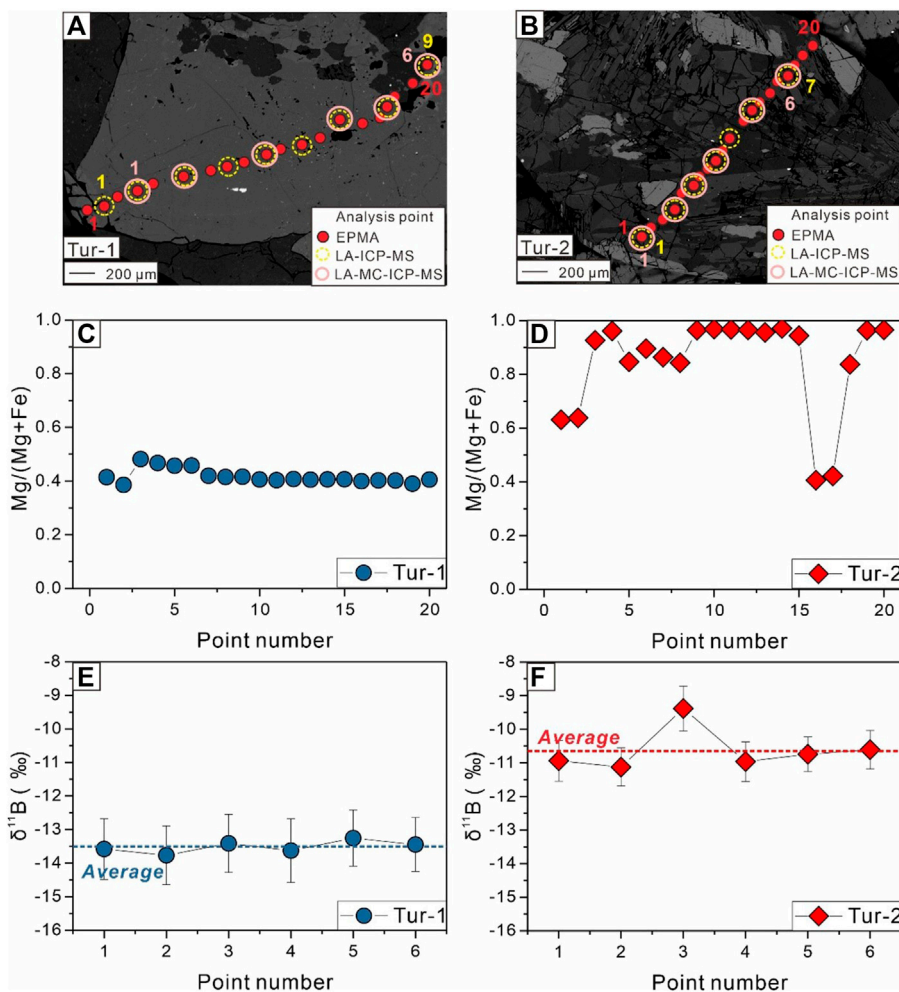
FIGURE 9
Composition changes in the tourmaline particle. **(A−B)** Analyzed point sites on the microscopic photograph; **(C−D)** change in the Mg/(Mg + Fe) ratio in the tourmaline particle; **(E−F)** change in the δ¹¹B value in the tourmaline particle.

and sphalerite. Moreover, compared with the GT group, the higher Eu/Eu* values and Sn content (Figures 6C,I) in Tur-1 and Tur-2 were coursed by the contribution of more oxidizing fluids, which is more favorable to lead to cassiterite precipitation.

5.3 Significance of the REE patterns of the hydrothermal tourmaline

For the hydrothermal tourmaline from the Cuonadong Sn–W–Be polymetallic deposit, there are two marked characteristics in the REE patterns of the hydrothermal vein (Tur-1) and skarn (Tur-2) (Figure 7).

1) Tur-2 has flat REE with weak LREE enrichment patterns, whereas those of Tur-1 are left-upward with strong LREE enrichment.

HREE can be more easily leached than LREE from granites and gneisses during high water–rock reactions due to hydrothermal mobilization of HREE from the granitic surrounding rock by plagioclase dissolution, releasing more HREE than LREE (Shibata et al., 2006; Marks et al., 2013). However, this is in line with the right inclined shape of the REE patterns of Tur-1, and we conclude that the shape of the REE patterns for hydrothermal tourmalines reflects the REE systematics of the fluids from which they crystallized with limited influence from the granitic surrounding rock. This implies that the REE contents of these hydrothermal fluids were unlikely controlled by the alteration of minerals in the surrounding gneisses. Tur-1 essentially inherited the REE characteristics of the ore-forming fluid released during the evolution of granitic magma. Meanwhile, the depletion of HREEs in Tur-1 and REEs in Tur-2 can be caused by the widespread co-crystallization of REE-rich minerals, particularly garnet, zircon, rutile, and apatite, during the late stage of hydrothermal activity and skarnization.
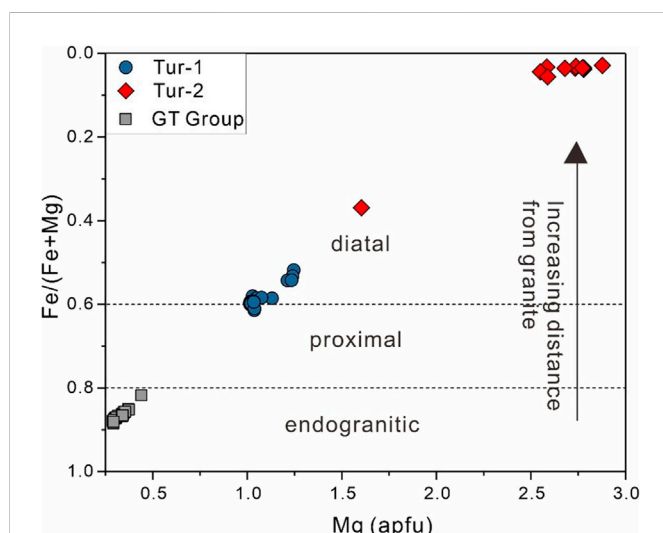
FIGURE 10
Fe/(Fe + Mg) vs. Mg diagram of the tourmaline from the Cuonadong Sn–W–Be polymetallic deposit, indicating the traveling distance of tourmaline-forming hydrothermal fluids. The compositions of the magmatic tourmaline in the leucogranite in the Xianglin area (GT group, gray square) are obtained from Xie et al. (2022).

2) Both Tur-1 and Tur-2 have obvious positive Eu anomalies.

Experimental studies concluded that tourmaline prefers Eu^{2+} over Eu^{3+} (van Hinsberg, 2011). It is noteworthy that Eu depletion in the granite and marble is inconsistent with the positive Eu anomaly in the hydrothermal fluid for Tur-1 and Tur-2. The addition of Eu to the magmatic-hydrothermal fluid could have been an alternative explanation for the positive Eu anomalies in the hydrothermal tourmaline. Positive Eu anomalies in the late hydrothermal minerals might be attributed to water–rock interactions (Zhao et al., 2019; Harlaux et al., 2020), similar to the positive Eu anomaly in scheelite from skarn (Dai et al., 2022). Intense water–rock interactions are supported by widespread skarnization and greisenization in the Cuonadong area (Dai et al., 2022; Wang et al., 2022). However, water–rock interactions between the original magmatic-hydrothermal fluid and the marble stratum could not have led to tourmaline formation with a positive Eu anomaly because all of them have a negative Eu anomaly. In contrast, plagioclase in the granite tends to be altered into sericite, thereby supplying Eu^{2+} to the ore-forming fluid with a strong water–rock reaction during magmatic-hydrothermal evolution by greisenization and skarnization (Zhao et al., 2019; Harlaux et al., 2020; Hu and Jiang, 2020). This process would enhance the Eu^{2+} concentration of the ore-forming fluids for the hydrothermal veins and skarn. Therefore, the addition of Eu^{2+} to the ore-forming fluids due to the hydrothermal alteration of the early rock-forming mineral during the late hydrothermal stage was probably the main cause for the generation of a positive Eu anomaly in Tur-1 and Tur-2.

5.3.1 Boron isotope defining the water−rock reaction

The results of fluid inclusion micro-thermometry from quartz, fluorite, calcite, and cassiterite indicate that the temperatures of the hydrothermal fluids of the Cuonadong polymetallic deposit range from 311°C to 319°C (an average of 315°C) and 232°C–361°C (an average of 351°C) in the cassiterite-bearing quartz vein and prograde skarn during the mineralization stage (Cao et al., 2021). The hydrothermal tourmalines have distinct $\delta^{11}B$ values: the $\delta^{11}B$ values of Tur-1 are −13.7 to −13.2‰ (an average of −13.5‰), whereas Tur-2 has higher $\delta^{11}B$ values (−11.1 to −9.3‰, an average of −10.6‰) (Figures 9, 10). In terms of the equilibrium fluid–tourmaline fractionations ($\Delta^{11}B_{fluid-tour}$) at 315°C and 351°C being at least 3.6‰ and 3.2‰, respectively (Meyer et al., 2008), our calculation results of the $\delta^{11}B_{fluid}$ values of ore-forming fluids range for Tur-1 and Tur-2 were between −10.1 to −9.6‰ and −7.9 to −6.1‰, respectively.

There is little B isotope fractionation between the melt and exsolution fluid in the granitic magma system (Meyer et al., 2008; Zhao et al., 2019). The $\delta^{11}B_{fluid}$ values of Tur-1 from −10.1 to −9.6‰ are close to the tourmaline $\delta^{11}B$ values (−8.7 to −8.0‰) of leucogranite in the Xianglin area (Xie et al., 2022), which suggest their closely genetic relationship (Figure 7). The B isotope characteristics of the granitoid in the Cuonadong polymetallic deposit indicate that it was mainly derived from partial melting of a metasediment source. This is also consistent with the Sr–Nd isotopic characteristic and high-K calc–alkaline and peraluminous characteristic of the Cuonadong granitoid (Xie et al., 2018; Xie et al., 2020; Chen et al., 2021). Furthermore, the whole Tur-1 from the rim to the core shows constant Mg/(Mg + Fe) and $\delta^{11}B$ values,

which indicates that the fluid composition was stable during Tur-1 formation (Figures 8, 9).

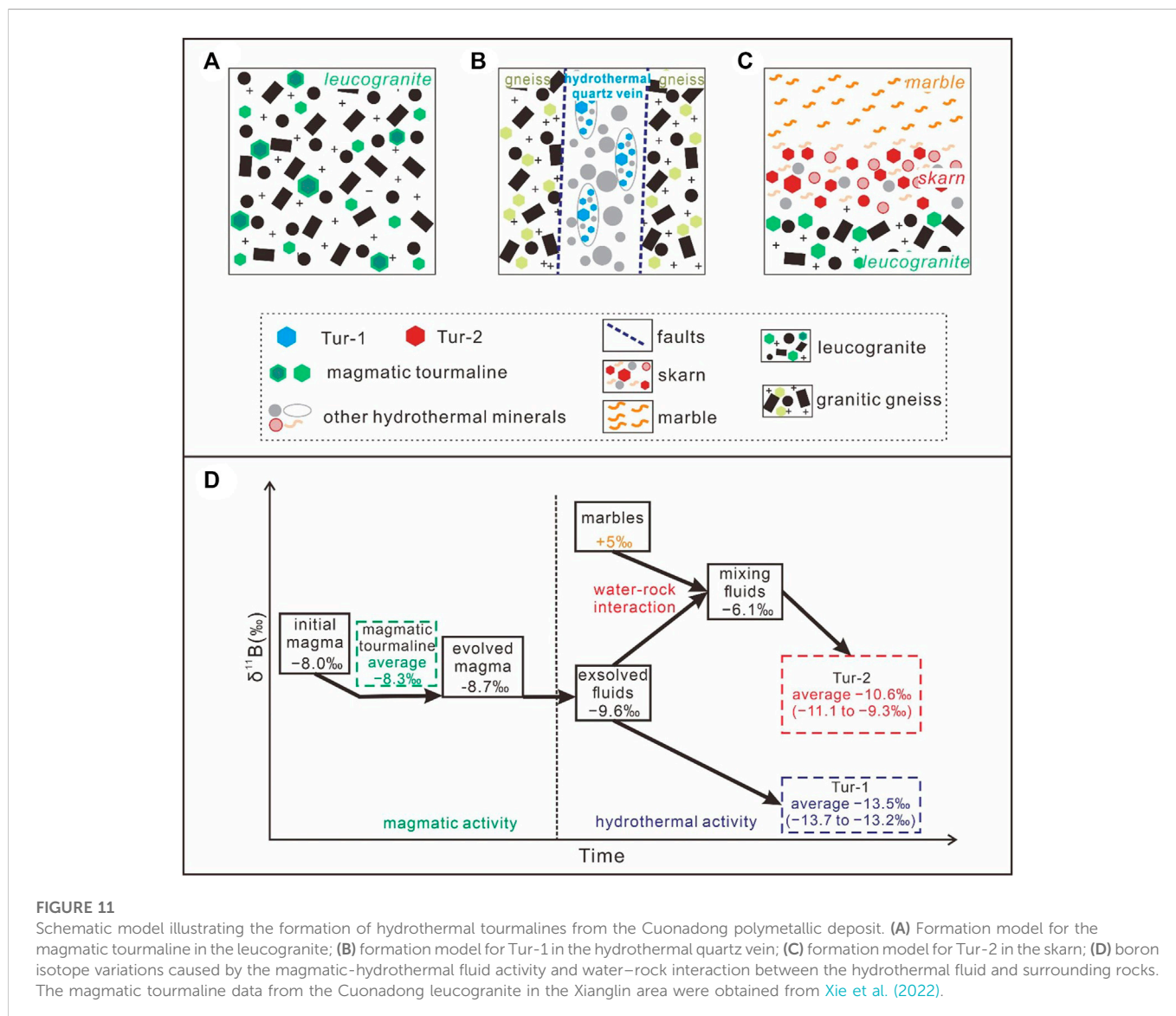Boron isotope signatures of Tur-2 ($\delta^{11}B$ =−11.1 to −9.3‰; calculated $\delta^{11}B_{fluid}$ =−7.9 to −6.1‰), higher than those in the leucogranitic melt, preclude the possibility of a single boron source of the leucogranite (average $\delta^{11}B$ = −8.3‰) (Xie et al., 2022) and suggest that the other sources with high $\delta^{11}B$ values were needed. The possible high $\delta^{11}B$ sources involved in the fluid of Tur-2 included seawater, evaporite, and marine carbonate (Marschall and Jiang, 2011; Trumbull and Slack, 2018). No seawater or evaporite was reported in/around the Cuonadong area; thus, they were unable to be a heavy B source for Tur-2. Instead, we propose that the B isotope signatures of Tur-2 could have been formed by the mixing of marble with the original magmatic-hydrothermal fluids because (1) Tur-2 was formed in a high-temperature condition (average 351 °C) (Cao et al., 2021), indicating the contribution of a synchronous magmatic source during magmatic-hydrothermal activity and (2) skarnization with strong hydrothermal metasomatism was ubiquitous in the marble stratum (Cao et al., 2021; Dai et al., 2022; Wang et al., 2022). In order to qualify their influence, we performed the model calculation. The Tethyan Himalaya leucogranites

(average B concentrations and $\delta^{11}B$ values of 144 ppm and −8.3‰, respectively) (Wu et al., 2020; Xie et al., 2022) and marble (65.4 ppm and +5.00‰) (Xavier et al., 2008; EarthChem, 2022) were used as the two end-members, and the model equation is as follows:

$$\delta^{11}B_{fluid-Tur-2} = \frac{m_1 f_1}{m_1 f_1 + m_2 (1-f_1)} \times \delta^{11}B_1 + \frac{m_2 (1-f_1)}{m_1 f_1 + m_2 (1-f_1)} \times \delta^{11}B_2,$$

where $\delta^{11}B_1$, $\delta^{11}B_2$, and $\delta^{11}B_{fluid-Tur-2}$ represent the B isotope values for the Tethyan Himalaya leucogranite, marble stratum, and the mixing fluid for Tur-2, respectively; m_1 and m_2 represent the molality of B in the Tethyan Himalayan leucogranite and marble, respectively.

The model calculations indicate that the formation of Tur-2 (max $\delta^{11}B_{fluid}$ value of −6.1‰) needs f_2 values to be 30.3%, suggesting that a small amount of marble is involved in the formation of Tur-2, compared with the magmatic-hydrothermal fluid. A schematic model is used to illustrate the formation of tourmalines from the Cuonadong polymetallic deposit and the boron isotope variations from magmatic to hydrothermal tourmalines (Figure 11).

FIGURE 11
Schematic model illustrating the formation of hydrothermal tourmalines from the Cuonadong polymetallic deposit. **(A)** Formation model for the magmatic tourmaline in the leucogranite; **(B)** formation model for Tur-1 in the hydrothermal quartz vein; **(C)** formation model for Tur-2 in the skarn; **(D)** boron isotope variations caused by the magmatic-hydrothermal fluid activity and water−rock interaction between the hydrothermal fluid and surrounding rocks. The magmatic tourmaline data from the Cuonadong leucogranite in the Xianglin area were obtained from Xie et al. (2022).

5.4 Implications for metal enrichment and mineralization

Tourmaline can host considerable amounts of Sn at the Y site through substitution (Harlaux et al., 2020). The Sn content of Tur-1 ranges from 24.1 ppm to 40.7 ppm (average = 32.1 ppm), which is close to the content in the Cuonadong two-mica granite (Sn = 15.7–29.9 ppm) (Huang et al., 2018; Xie et al., 2018; Cao et al., 2020) (Figures 5, 6C). The Sn distribution coefficients in the tourmaline–silicate melt and fluid–melt are nearly 1 (van Hinsberg, 2011) and 1–6 (Zajacz et al., 2008; Schmidt et al., 2020), respectively. Hence, the same Sn contents in the two-mica granite and hydrothermal vein indicate that the fluid exsolution and upwelling from the fault did not lead to a large amount of Sn enrichment in this study. This may control the condition of the ore-forming fluid. This also shows the importance of highly evolved magma to Sn ore-forming magma.

The Sn content can be continuously enriched during magmatic evolution and then partitioned into minerals, such as cassiterite (Schmidt et al., 2020; Xiang et al., 2020). A small amount of Sn can be preserved in the lattice of early rock-forming minerals, such as garnet (Yu et al., 2020). Increased Sn contents in the late-stage hydrothermal tourmaline possibly reflect magmatic-hydrothermal evolution (Zhao et al., 2019; Harlaux et al., 2020) or/and hydrothermal fluid leaching the early minerals through water–rock interactions (Harlaux et al., 2020). The highest Sn contents in Tur-2 in the skarn, which range from 102 to 183 ppm, are higher than those in Tur-1 and two-mica granite in the Cuonadong dome (Figure 6C). This is consistent with the extensive water–rock reactions during late-stage skarnization, which enriched Sn by leaching early minerals (Xiang et al., 2018; Xiang et al., 2020; Cao et al., 2021; Wang et al., 2022) and recorded it in Tur-2.

Li and Be are incompatible elements in most rock-forming minerals and tend to remain in the melt during fractional crystallization with tourmaline–melt partition coefficients of 0.89 and 0.44, respectively (van Hinsberg, 2011). An increase in the Li and Be contents of the tourmaline can record progressive Li and Be enrichment during magmatic evolution (Zhu et al., 2020). The Li and Be contents will also increase from magma to hydrothermal fluids due to two processes: (1) melt–fluid separation (Liu et al., 2020; Wang et al., 2022) and (2) water–rock interaction (Xiang et al., 2020; Wang et al., 2022). In the exsolution process of the magmatic-hydrothermal fluid, Li and Be are enriched in the fluid because of their higher incompatibility. The mobilization of Li and Be from the surrounding gneiss and marble by hydrothermal activity, which has substantial Li (an average of 32.5 and 46.6 ppm, respectively) and Be (an average of 2.34 and 3.23 ppm, respectively) contents (EarthChem, 2022), can also contribute to the high Li and Be contents in the hydrothermal tourmaline. Importantly, Tur-2 in skarn involved more surrounding rock materials and has higher Li and Be contents than Tur-1 in the hydrothermal quartz vein in this study and the magmatic tourmaline from the leucogranite (Figures 6A,B). Hence, late Li and Be enrichment in the skarn was related to the strong water–rock reaction among the fluid, the early hydrothermal minerals, and surrounding rock.

6 Conclusion

The texture and geochemical compositions suggest that Tur-1 in the hydrothermal vein was formed from a magmatic-hydrothermal fluid with little influence from the surrounding rock, whereas Tur-2 in the skarn involved more fluid from surrounding rocks. The contents of ore-forming elements in the two types of tourmalines indicate that the reaction between the magmatic exsolution fluid and the surrounding rock is essential for the enrichment and precipitation of ore-forming elements.

Data availability statement

The original contributions presented in the study are included in the article/Supplementary Material; further inquiries can be directed to the corresponding author.

Author contributions

LZ designed the research; LZ, GX, HY, KW, and RZ performed the research; GX analyzed the data; GX wrote the original draft; GX, LZ, HY, KW, and RZ reviewed and edited the manuscript.

Funding

Acknowledgments

Conflict of interest

The authors declare that the research was conducted in the absence of any commercial or financial relationships that could be construed as a potential conflict of interest.

Publisher's note

All claims expressed in this article are solely those of the authors and do not necessarily represent those of their affiliated organizations, or those of the publisher, the editors, and the reviewers. Any product that may be evaluated in this article, or claim that may be made by its manufacturer, is not guaranteed or endorsed by the publisher.

Supplementary material

The Supplementary Material for this article can be found online at: https://www.frontiersin.org/articles/10.3389/feart.2023.1106871/full#supplementary-material

References

Abedini, A., Rezaei Azizi, M., and Dill, H. G. (2020). The tetrad effect in REE distribution patterns: A quantitative approach to genetic issues of argillic and propylitic alteration zones of epithermal Cu-Pb-Fe deposits related to andesitic magmatism (khan kandi district, NW Iran). *J. Geochem. Explor.* 212, 106516. doi:10.1016/j.gexplo.2020.106516

Audtat, A., Gnther, D., and Heinrich, C. A. (2000). Magmatic-hydrothermal evolution in a fractionating granite: A microchemical study of the Sn-W-F-mineralized mole granite (Australia). *Geochim. Cosmochim. Acta* 64 (19), 3373–3393. doi:10.1016/S0016-7037(00)00428-2

Burg, J. P., and Bouilhol, P. (2019). Timeline of the South Tibet – Himalayan belt: the geochronological record of subduction, collision, and underthrusting from zircon and monazite U–Pb ages. *Can. J. Earth Sci.* 56 (12), 1318–1332. doi:10.1139/cjes-2018-0174

Cao, H. W., Huang, Y., Li, G. M., Zhang, L. K., Wu, J. Y., Dong, L., et al. (2018). Late triassic sedimentary records in the northern tethyan Himalaya: Tectonic link with greater India. *Geosci. Front.* 9 (1), 273–291. doi:10.1016/j.gsf.2017.04.001

Cao, H. W., Li, G. M., Zhang, Z., Zhang, L. K., Dong, S. L., Xia, X. B., et al. (2020). Miocene Sn polymetallic mineralization in the tethyan Himalaya, southeastern Tibet: A case study of the Cuonadong deposit. *Ore Geol. Rev.* 119, 103403. doi:10.1016/j.oregeorev.2020.103403

Cao, H. W., Li, G. M., Zhang, R. Q., Zhang, Y. H., Zhang, L. K., Dai, Z. W., et al. (2021). Genesis of the Cuonadong tin polymetallic deposit in the tethyan Himalaya: evidence from geology, geochronology, fluid inclusions and multiple isotopes. *Gondwana Res.* 92, 72–101. doi:10.1016/j.gr.2020.12.020

Cao, H. W., Pei, Q. M., Santosh, M., Li, G. M., Zhang, L. K., Zhang, X. F., et al. (2022). Himalayan leucogranites: A review of geochemical and isotopic characteristics, timing of formation, Genesis, and rare metal mineralization. *Earth Sci. Rev.* 234, 104229. doi:10.1016/j.earscirev.2022.104229

Chakraborty, T. (2021). Tourmaline growth and evolution in S-type granites and pegmatites: constraints from textural, chemical and B-isotopic study from the gangpur schist belt granitoids, eastern India. *Geol. Mag.* 158 (9), 1657–1670. doi:10.1017/S0016756821000224

Chen, X., Zhang, G., Gao, R., Zhang, D., and Yang, B. (2021). Petrogenesis of highly fractionated leucogranite in the himalayas: the early Miocene Cuonadong example. *Geol. J.* 56 (7), 3791–3807. doi:10.1002/gj.4126

Dai, Z. W., Li, G. M., Ding, J., Zhang, L. K., Cao, H. W., Zhang, Z., et al. (2019). Chemical and boron Isotopic composition, and significance of tourmaline from the Cuonadong tourmaline granite, Tibet. *Earth Sci.* 44 (6), 1849–1859. doi:10.3799/dqkx.2019.043

Dai, Z. W., Li, G. M., Xie, Y. L., Yang, Z. M., Marten Huizenga, J., Liang, W., et al. (2022). Source and evolution of the ore-forming fluid of the Cuonadong Sn-W-Be polymetallic deposit (southern Tibet, China): constraints from scheelite trace element and Sr isotope geochemistry. *Ore Geol. Rev.* 142, 104570. doi:10.1016/j.oregeorev.2021.104570

Daver, L., Jébrak, M., Beaudoin, G., and Trumbull, R. B. (2020). Three-stage formation of greenstone-hosted orogenic gold deposits in the Val-d'Or mining district, Abitibi, Canada: Evidence from pyrite and tourmaline. *Ore Geol. Rev.* 120, 103449. doi:10.1016/j.oregeorev.2020.103449

Dong, H. W., Xu, Z. Q., Meng, Y. K., and Yi, Z. Y. (2017). Geochronology of leucogranites in the Cuonadong dome, southern Tibet and limitation of the timing of the southern Tibet detachment system (STDS). *Acta Petrol. Sin.* 33 (12), 3741–3752.

Dutrow, B. L., and Henry, D. J. (2016). Fibrous tourmaline: A sensitive Probe of fluid compositions and petrologic environments. *Can. Mineral.* 54 (1), 311–335. doi:10.3749/canmin.1600019

Dutrow, B. L., and Henry, D. J. (2018). Tourmaline compositions and textures: reflections of the fluid phase. *J. Geosci.* 63 (2), 99–110. doi:10.3190/jgeosci.256

EarthChem (2022). Born content in the marble. Available in: http://www.earthchem.org/portal.(Accessed October 07, 2022)

Fu, J., Li, G., Wang, G., Zhang, L., Liang, W., Zhang, Z., et al. (2018). Synchronous granite intrusion and E–W extension in the Cuonadong dome, southern Tibet, China: evidence from field observations and thermochronologic results. *Int. J. Earth Sci.* 107 (6), 2023–2041. doi:10.1007/s00531-018-1585-y

Goscombe, B., Gray, D., and Foster, D. A. (2018). Metamorphic response to collision in the central himalayan orogen. *Gondwana Res.* 57, 191–265. doi:10.1016/j.gr.2018.02.002

Han, J., Hollings, P., Jourdan, F., Zeng, Y., and Chen, H. (2020). Inherited Eocene magmatic tourmaline captured by the Miocene Himalayan leucogranites. *Am. Mineral.* 105 (9), 1436–1440. doi:10.2138/am-2020-7608

Harlaux, M., Kouzmanov, K., Gialli, S., Laurent, O., Rielli, A., Dini, A., et al. (2020). Tourmaline as a tracer of late-magmatic to hydrothermal fluid evolution: the world-class san rafael tin (-copper) deposit, Peru. *Econ. Geol.* 115 (8), 1665–1697. doi:10.5382/econgeo.4762

Hazarika, P., Bhuyan, N., Upadhyay, D., Abhinay, K., and Singh, N. N. (2019). The nature and sources of ore-forming fluids in the bhukia gold deposit, western India: constraints from chemical and boron isotopic composition of tourmaline. *Lithos* 350-351, 105227–105351. doi:10.1016/j.lithos.2019.105227

Henry, D. J., and Dutrow, B. L. (2018). Tourmaline studies through time: contributions to scientific advancements. *J. Geosci.*, 77–98. doi:10.3190/jgeosci.255

Henry, D. J., Novak, M., Hawthorne, F. C., Ertl, A., Dutrow, B. L., Uher, P., et al. (2011). Nomenclature of the tourmaline-supergroup minerals. *Am. Mineral.* 96 (5-6), 895–913. doi:10.2138/am.2011.3636

Hou, K. J., Li, Y. H., Xiao, Y. K., Liu, F., and Tian, Y. R. (2010). *In situ* boron isotope measurements of natural geological materials by LA-MC-ICP-MS. *Sci. Bull.* 55 (29), 3305–3311. doi:10.1007/s11434-010-4064-9

Hu, D. L., and Jiang, S. Y. (2020). *In-situ* elemental and boron isotopic variations of tourmaline from the maogongdong deposit in the dahutang W-Cu ore field of northern jiangxi province, south China: Insights into magmatic-hydrothermal evolution. *Ore Geol. Rev.* 122, 103502. doi:10.1016/j.oregeorev.2020.103502

Hu, X., Garzanti, E., Wang, J., Huang, W., An, W., and Webb, A. (2016). The timing of India-Asia collision onset – facts, theories, controversies. *Earth Sci. Rev.* 160, 264–299. doi:10.1016/j.earscirev.2016.07.014

Huang, C., Li, G., Zhang, Z., Liang, W., Huang, Y., Zhang, L., et al. (2018). Petrogenesis of the Cuonadong leucogranite in south Tibet: constraints from bulk-rock geochemistry and zircon U-Pb dating. *Earth Sci. Front.* 25 (6), 182–195. doi:10.13745/j.esf.sf.2018.11.2

Jiang, S. Y., and Palmer, M. R. (1998). Boron isotope systematics of tourmaline from granites and pegmatites: a synthesis. *Eur. J. Mineral.* 10 (6), 1253–1265. doi:10.1127/ejm/10/6/1253

Kohn, M. J. (2014). Himalayan metamorphism and its tectonic implications. *Annu. Rev. Earth Planet Sci.* 42 (1), 381–419. doi:10.1146/annurev-earth-060313-055005

Li, G., Dong, L., Huang, Y., Zhang, L., Jiao, Y., Xia, X., et al. (2017). First discovery and implications of Cuonadong superlarge Be-W-Sn polymetallic deposit in Himalayan metallogenic belt, southern Tibet. *Min. Depos.* 036 (004), 1003–1008. doi:10.16111/j.0258-7106.2017.04.014

Liang, W., Zhang, L., Xia, X., Ma, G., Huang, Y., Zhang, Z., et al. (2018). Geology and preliminary mineral Genesis of the Cuonadong W-Sn polymetallic deposit, Southern Tibet, China. *Earth Sci.* 43 (8), 2742. doi:10.3799/dqkx.2018.154

Liu, C., Wang, R. C., Wu, F. Y., Xie, L., Liu, X. C., Li, X. K., et al. (2020). Spodumene pegmatites from the pusila pluton in the higher Himalaya, south Tibet: Lithium mineralization in a highly fractionated leucogranite batholith. *Lithos* 358-359, 105421–106359. doi:10.1016/j.lithos.2020.105421

Marks, M. A. W., Marschall, H. R., Schühle, P., Guth, A., Wenzel, T., Jacob, D. E., et al. (2013). Trace element systematics of tourmaline in pegmatitic and hydrothermal systems from the variscan schwarzwald (Germany): the importance of major element composition, sector zoning, and fluid or melt composition. *Chem. Geol.* 344, 73–90. doi:10.1016/j.chemgeo.2013.02.025

Marschall, H. R., and Jiang, S. Y. (2011). Tourmaline isotopes: No element left behind. *Elements* 7 (5), 313–319. doi:10.2113/gselements.7.5.313

Melezhik, V. A., Roberts, D., Fallick, A. E., Gorokhov, I. M., and Kusnetzov, A. B. (2005). Geochemical preservation potential of high-grade calcite marble versus dolomite marble: Implication for isotope chemostratigraphy. *Chem. Geol.* 216 (3-4), 203–224. doi:10.1016/j.chemgeo.2004.11.020

Meyer, C., Wunder, B., Meixner, A., Romer, R. L., and Heinrich, W. (2008). Boron-isotope fractionation between tourmaline and fluid: An experimental re-investigation. *Contrib. Mineral. Petrol.* 156 (2), 259–267. doi:10.1007/s00410-008-0285-1

Mukherjee, P. K., Jain, A. K., Singhal, S., Singha, N. B., Singh, S., Kumud, K., et al. (2019). U-Pb zircon ages and Sm-Nd isotopic characteristics of the Lesser and Great Himalayan sequences, Uttarakhand Himalaya, and their regional tectonic implications. *Gondwana Res.* 75, 282–297. doi:10.1016/j.gr.2019.06.001

Najman, Y., Jenks, D., Godin, L., Boudagher-Fadel, M., Millar, I., Garzanti, E., et al. (2017). The Tethyan Himalayan detrital record shows that India–Asia terminal collision occurred by 54 Ma in the Western Himalaya. *Earth Planet. Sci. Lett.* 459, 301–310. doi:10.1016/j.epsl.2016.11.036

Pan, G., Wang, L., Li, R., Yuan, S., Ji, W., Yin, F., et al. (2012). Tectonic evolution of the qinghai-tibet plateau. *J. Asian Earth Sci.* 53, 3–14. doi:10.1016/j.jseaes.2011.12.018

Pei, Q., Ma, S., Li, C., Liu, F., Zhang, Y., Xiao, Y., et al. (2023). *In-situ* boron isotope and chemical composition of tourmaline in the Gyirong pegmatite, southern Tibet: Implications for petrogenesis and magma source. *Front. Earth Sci.* 1037727, 2190. doi:10.3389/feart.2022.1037727

Pirajno, F., and Smithies, R. H. (1992). The FeO/(FeO+MgO) ratio of tourmaline: A useful indicator of spatial variations in granite-related hydrothermal mineral deposits. *J. Geochem. Explor.* 42 (2), 371–381. doi:10.1016/0375-6742(92)90033-5

Rajabpour, S., Jiang, S. Y., Lehmann, B., Abedini, A., and Gregory, D. D. (2018). Fluid inclusion and O–H–C isotopic constraints on the origin and evolution of ore-forming fluids of the Cenozoic volcanic-hosted Kuh-Pang copper deposit, Central Iran. *Ore Geol. Rev.* 94, 277–289. doi:10.1016/j.oregeorev.2018.02.003

Rezaei Azizi, M., Abedini, A., Alipour, S., and Bagheri, H. (2018a). The laal-kan fluorite deposit, zanjan province, NW Iran: constraints on REE geochemistry and fluid inclusions. *Arab. J. Geosci.* 11 (22), 719. doi:10.1007/s12517-018-4055-8

Rezaei Azizi, M., Alipour, S., Abedini, A., and Bagheri, H. (2018b). REE geochemical characteristics and fluid inclusion studies of the Bagher-Abad fluorite deposit, Central Iran. *Neues Jahrb. fur Mineral. Abh.* 195, 247–263. doi:10.1127/njma/2018/0124

Rudnick, R. L., and Gao, S. (2003). "Composition of the continental crust," in *Treatise on Geochemistry. The crust*. Editors H. D. Holland and K. K. Turekian (Oxford: Elsevier-Pergamon), Vol. 3, 1–64.

Schmidt, C., Romer, R. L., Wohlgemuth Ueberwasser, C. C., and Appelt, O. (2020). Partitioning of Sn and W between granitic melt and aqueous fluid. *Ore Geol. Rev.* 117, 103263. doi:10.1016/j.oregeorev.2019.103263

Schmidt, C. (2018). formation of hydrothermal tin deposits: Raman spectroscopic evidence for an important role of aqueous Sn (IV) species. *Geochim. Cosmochim. Acta* 220, 499–511. doi:10.1016/j.gca.2017.10.011

Shibata, S. N., Tanaka, T., and Yamamoto, K. (2006). Crystal structure control of the dissolution of rare Earth elements in water-mineral interactions. *Geochem. J.* 40, 437–446. doi:10.2343/geochemj.40.437

Siahcheshm, K., Calagari, A., Abedini, A., and Sindern, S. (2014). Elemental mobility and mass changes during alteration in the Maher-Abad porphyry Cu–Au deposit, SW Birjand, Eastern Iran. *Period. Miner.* 83, 55–76. doi:10.2451/2014PM0004

Sun, S. S., and McDonough, W. F. (1989). Chemical and isotopic systematics of oceanic basalts: Implications for mantle composition and processes. *Geo.Soc.London Spec. Pub.* 42 (1), 313–345. doi:10.1144/gsl.Sp.1989.042.01.19

Trumbull, R. B., and Slack, J. F. (2018). "Boron isotopes in the continental crust: granites, pegmatites, felsic volcanic rocks, and related ore deposits," in *Boron isotopes. Advances in isotope Geochemistry*. Editors H. Marschall and G. Foster (Cham: Springer), 249–272.

Trumbull, R. B., Garda, G. M., Xavier, R. P., Cavalcanti, J. A. D., and Codeço, M. S. (2018). Tourmaline in the passagem de Mariana gold deposit (Brazil) revisited: major-element, trace-element and B-isotope constraints on metallogenesis. *Min. Depos.* 54 (3), 395–414. doi:10.1007/s00126-018-0819-z

Trumbull, R. B., Codeço, M. S., Jiang, S. Y., Palmer, M. R., and Slack, J. F. (2020). Boron isotope variations in tourmaline from hydrothermal ore deposits: A review of controlling factors and insights for mineralizing systems. *Ore Geol. Rev.* 125, 103682. doi:10.1016/j.oregeorev.2020.103682

van Hinsberg, V. J., Henry, D. J., and Dutrow, B. L. (2011a). Tourmaline as a petrologic forensic mineral: A unique recorder of its geologic past. *Elements* 7 (5), 327–332. doi:10.2113/gselements.7.5.327

van Hinsberg, V. J., Henry, D. J., and Marschall, H. R. (2011b). Tourmaline: An ideal indicator of its host environment. *Can. Mineral.* 49 (1), 1–16. doi:10.3749/canmin.49.1.1

van Hinsberg, V. J. (2011). Preliminary experimental data on trace-element partitioning between tourmaline and silicate melt. *Can. Mineral.* 49 (1), 153–163. doi:10.3749/canmin.49.1.153

Wang, R. C., Wu, F. Y., Xie, L., Liu, X. C., Wang, J. M., Yang, L., et al. (2017). A preliminary study of rare-metal mineralization in the Himalayan leucogranite belts, South Tibet. *Sci. China Earth Sci.* 60 (9), 1655–1663. doi:10.1007/s11430-017-9075-8

Wang, Y., Li, G., Liang, W., and Zhang, Z. (2022). The chemical characteristics and metallogenic mechanism of beryl from Cuonadong Sn-W-Be rare polymetallic deposit in Southern Tibet, China. *Minerals* 12 (5), 497. doi:10.3390/min12050497

Wu, F. Y., Liu, Z. C., Liu, X. C., and Ji, W. Q. (2015). Himalayan leucogranite: petrogenesis and implications to orogenesis and plateau uplift. *Acta Petrol. Sin.* 31 (1), 1–36.

Wu, F. Y., Liu, X. C., Liu, Z. C., Wang, R. C., Xie, L., Wang, J. M., et al. (2020). Highly fractionated Himalayan leucogranites and associated rare-metal mineralization. *Lithos* 352, 105319. doi:10.1016/j.lithos.2019.105319

Xavier, R. P., Wiedenbeck, M., Trumbull, R. B., Dreher, A. M., Monteiro, L. V. S., Rhede, D., et al. (2008). Tourmaline B-isotopes fingerprint marine evaporites as the source of high-salinity ore fluids in iron oxide copper-gold deposits, Carajas Mineral Province (Brazil). *Geology* 36 (9), 743–746. doi:10.1130/G24841A.1

Xia, X., Li, G., Cao, H., Liang, W., and Fu, J. (2019a). Petrogenic age and geochemical characteristics of the mother rock of skarn type ore body in the Cuonadong Be-W-Sn polymetallic deposit, Southern Tibet. *Earth Sci.* 44 (7), 2207–2223. doi:10.3799/dqkx.2019.038

Xia, X., Xiang, A., Li, G. M., Zhang, L. K., Cao, H., Zhang, Z., et al. (2019b). Neoproterozoic magmatism of Cuonadong dome and its tectonic implication, Tibet. *China. J. Chengdu Univ. Technol.* 46, 435–448. doi:10.3969/j.issn.1671-9727.2019.04.04

Xiang, L., Wang, R. C., Erdmann, S., Sizaret, S., Lu, J. J., Zhang, W. L., et al. (2018). Neoproterozoic mineralization in a hydrothermal cassiterite-sulfide deposit at jiumao, northern guangxi, south China: mineral-scale constraints on metal origins and ore-forming processes. *Ore Geol. Rev.* 94, 172–192. doi:10.1016/j.oregeorev.2018.01.013

Xiang, L., Romer, R. L., Glodny, J., Trumbull, R. B., and Wang, R. (2020). Li and B isotopic fractionation at the magmatic-hydrothermal transition of highly evolved granites. *Lithos* 376-377, 105753. doi:10.1016/j.lithos.2020.105753

Xie, J., Qiu, H., Bai, X., Zhang, W., Wang, Q., and Xia, X. (2018). Geochronological and geochemical constraints on the Cuonadong leucogranite, eastern Himalaya. *Acta Geochim.* 37 (3), 347–359. doi:10.1007/s11631-018-0273-8

Xie, L., Tao, X., Wang, R. C., Wu, F. Y., Liu, C., Liu, X., et al. (2020). Highly fractionated leucogranites in the eastern Himalayan Cuonadong dome and related magmatic Be–Nb–Ta and hydrothermal Be–W–Sn mineralization. *Lithos* 354-355, 105286. doi:10.1016/j.lithos.2019.105286

Xie, G., Yan, H., Li, G., Guo, J., Liu, F., Chen, Q., et al. (2022). Elemental and boron isotopic variations in tourmaline in two-mica granite from the cuona area, Tibet: Insights into the evolution of leucogranitic melt. *Geochemistry*, 125924. doi:10.1016/j.chemer.2022.125924

Yang, S. Y., and Jiang, S. Y. (2012). Chemical and boron isotopic composition of tourmaline in the xiangshan volcanic-intrusive complex, southeast China: evidence for boron mobilization and infiltration during magmatic-hydrothermal processes. *Chem. Geol.* 312, 177–189. doi:10.1016/j.chemgeo.2012.04.026

Yang, S. Y., Jiang, S. Y., and Palmer, M. R. (2015a). Chemical and boron isotopic compositions of tourmaline from the Nyalam leucogranites, South Tibetan Himalaya: Implication for their formation from B-rich melt to hydrothermal fluids. *Chem. Geol.* 419, 102–113. doi:10.1016/j.chemgeo.2015.10.026

Yang, S. Y., Jiang, S. Y., Zhao, K. D., Dai, B. Z., and Yang, T. (2015b). Tourmaline as a recorder of magmatic–hydrothermal evolution: An *in situ* major and trace element analysis of tourmaline from the qitianling batholith, south China. *Contrib. Mineral. Petrol.* 170 (5), 42. doi:10.1007/s00410-015-1195-7

Yin, A., and Harrison, T. M. (2000). Geologic evolution of the himalayan-Tibetan orogen. *Annu. Rev. Earth Planet. Sci.* 28 (1), 211–280. doi:10.1146/annurev.earth.28.1.211

Yin, A. (2006). Cenozoic tectonic evolution of the Himalayan orogen as constrained by along-strike variation of structural geometry, exhumation history, and foreland sedimentation. *Earth Sci. Rev.* 76 (1-2), 1–131. doi:10.1016/j.earscirev.2005.05.004

Yu, F., Shu, Q., Niu, X., Xing, K., Li, L., Lentz, D. R., et al. (2020). Composition of garnet from the xianghualing skarn Sn deposit, south China: Its petrogenetic significance and exploration potential. *Minerals* 10 (5), 456. doi:10.3390/min10050456

Zajacz, Z., Halter, W. E., Pettke, T., and Guillong, M. (2008). Determination of fluid/melt partition coefficients by LA-ICPMS analysis of co-existing fluid and silicate melt inclusions: Controls on element partitioning. *Geochim. Cosmochim. Acta* 72 (8), 2169–2197. doi:10.1016/j.gca.2008.01.034

Zhang, Z., Zhang, L. K., Li, G. M., Liang, W., Xia, X. B., Fu, J. G., et al. (2017). The Cuonadong gneiss dome of North Himalaya: A new member of gneiss dome and a new proposition for the ore-controlling role of North Himalaya gneiss domes. *Acta Geosci. Sin.* (5), 754–766. doi:10.3975/cagsb.2017.05.15

Zhang, L., Zhang, Z., Li, G., Dong, S., Xia, X., Liang, W., et al. (2018). Rock assemblage, structural characteristics and Genesis mechanism of the Cuonadong dome, Tethys Himalaya. *Earth Sci.* 43 (8), 2664. doi:10.3799/dqkx.2018.141

Zhang, W., Chen, H., Peng, L., Zhao, L., Huang, J., Lu, W., et al. (2018). Discriminating hydrothermal fluid sources using tourmaline boron isotopes: example from bailingshan Fe deposit in the eastern tianshan, NW China. *Ore Geol. Rev.* 98, 28–37. doi:10.1016/j.oregeorev.2018.05.015

Zhang, L., Li, G., Cao, H., Zhang, Z., Fu, J., Xia, X., et al. (2019). Zircon geochronology and Hf isotope compositions of the granitic gneiss from Cuonadong in South Tibet and its insights for the evolution of the Proto-Tethys. *Geol. China* 46 (6), 1312–1335. doi:10.12029/gc20190606

Zhang, L. K., Li, G. M., Santosh, M., Cao, H. W., Dong, S. L., Zhang, Z., et al. (2019). Cambrian magmatism in the Tethys Himalaya and implications for the evolution of the proto-tethys along the northern gondwana margin: A case study and overview. *Geol. J.* 54 (4), 2545–2565. doi:10.1002/gj.3311

Zhao, H. D., Zhao, K. D., Palmer, M. R., and Jiang, S. Y. (2019). *In-situ* elemental and boron isotopic variations of tourmaline from the Sanfang granite, South China: Insights into magmatic-hydrothermal evolution. *Chem. Geol.* 504, 190–204. doi:10.1016/j.chemgeo.2018.11.013

Zhao, Z., Yang, X., Zhang, T., Lu, Y., Li, W., and Zhang, Z. (2022). Geochemical characteristics and boron isotopes of tourmaline from the baishaziling tin deposit, nanling Range: constraints on magmatic-hydrothermal processes. *Ore Geol. Rev.* 142, 104695. doi:10.1016/j.oregeorev.2022.104695

Zheng, Y., and Wu, F. (2018). The timing of continental collision between India and Asia. *Sci. Bull.* 63 (24), 1649–1654. doi:10.1016/j.scib.2018.11.022

Zheng, Z., Chen, Y., Deng, X., Yue, S., Chen, H., and Wang, Q. (2019). Tourmaline geochemistry and boron isotopic variations as a guide to fluid evolution in the Qiman Tagh W–Sn belt, East Kunlun, China. *Geosci. Front.* 10 (2), 569–580. doi:10.1016/j.gsf.2018.04.007

Zhou, Q., Li, W., Wang, G., Liu, Z., Lai, Y., and Huang, J. (2019). Chemical and boron isotopic composition of tourmaline from the Conadong leucogranite-pegmatite system in South Tibet. *Lithos* 326–327, 529–539. doi:10.1016/j.lithos.2019.01.003

Zhu, X., Raschke, M. B., and Liu, Y. (2020). Tourmaline as a recorder of ore-forming processes in the xuebaoding W-Sn-Be deposit, sichuan province, China: evidence from the chemical composition of tourmaline. *Minerals* 10 (5), 438. doi:10.3390/min10050438